PHYSICAL REVIEW FLUIDS **2**, 094606 (2017)

Lyapunov exponent as a metric for assessing the dynamic content and predictability of large-eddy simulations

Gabriel Nastac, Jeffrey W. Labahn, Luca Magri, and Matthias Ihme[*]

Center for Turbulence Research, Stanford University, Stanford, California, USA

(Received 16 February 2017; published 21 September 2017)

Metrics used to assess the quality of large-eddy simulations commonly rely on a statistical assessment of the solution. While these metrics are valuable, a dynamic measure is desirable to further characterize the ability of a numerical simulation for capturing dynamic processes inherent in turbulent flows. To address this issue, a dynamic metric based on the Lyapunov exponent is proposed which assesses the growth rate of the solution separation. This metric is applied to two turbulent flow configurations: forced homogeneous isotropic turbulence and a turbulent jet diffusion flame. First, it is shown that, despite the direct numerical simulation (DNS) and large-eddy simulation (LES) being high-dimensional dynamical systems with $O(10^7)$ degrees of freedom, the separation growth rate qualitatively behaves like a lower-dimensional dynamical system, in which the dimension of the Lyapunov system is substantially smaller than the discretized dynamical system. Second, a grid refinement analysis of each configuration demonstrates that as the LES filter width approaches the smallest scales of the system the Lyapunov exponent asymptotically approaches a plateau. Third, a small perturbation is superimposed onto the initial conditions of each configuration, and the Lyapunov exponent is used to estimate the time required for divergence, thereby providing a direct assessment of the predictability time of simulations. By comparing inert and reacting flows, it is shown that combustion increases the predictability of the turbulent simulation as a result of the dilatation and increased viscosity by heat release. The predictability time is found to scale with the integral time scale in both the reacting and inert jet flows. Fourth, an analysis of the local Lyapunov exponent is performed to demonstrate that this metric can also determine flow-dependent properties, such as regions that are sensitive to small perturbations or conditions of large turbulence within the flow field. Finally, it is demonstrated that the global Lyapunov exponent can be utilized as a metric to determine if the computational domain is large enough to adequately encompass the dynamic nature of the flow.

DOI: 10.1103/PhysRevFluids.2.094606

I. INTRODUCTION

Direct numerical simulation (DNS) and large-eddy simulation (LES) have been employed for computing the dynamics of turbulent flows. While DNS resolves all turbulent scales involved in the dynamics with no physical modeling, LES represents the energy contained in the large scales, and the effect of the smaller scales is taken into account either explicitly through a subgrid scale model, or implicitly through the dissipation of the numerical method. Besides numerical algorithms, two factors determine the quality of LES: the physical model or dissipation of the subgrid scales (SGSs), which are filtered out in the governing equations, and the filter width, which describes the numerical resolution of the resolved scales.

Assessing the quality of LES has been the subject of numerous studies [1–4]. A common way to perform a grid refinement is to observe that the statistics are converging. Although this is possible for Reynolds-Averaged Navier-Stokes (RANS) and laminar flows, an issue arises for unsteady turbulent flows. Specifically, the modeled equations in LES introduce a dependence on the filter width so

---

[*] mihme@stanford.edu

that evaluating the quality of the simulation is particularly challenging. Quality is defined as how well LES predicts smooth quantities correctly with respect to a DNS solution, the latter of which is often not available, hence, the problem of finding suitable measures of the quality of LES. Current metrics used in determining LES quality address this problem by utilizing a statistical assessment of the solution, considering mean-flow quantities and higher-order statistical moments. One commonly used statistical metric is Pope's criterion [1],

$$M = \frac{k_{\mathrm{sgs}}}{k_{\mathrm{res}} + k_{\mathrm{sgs}}}, \tag{1}$$

which is the ratio of subgrid turbulent kinetic energy, k_{sgs}, over the total turbulent kinetic energy, being the sum of the subgrid turbulent kinetic energy and the resolved turbulent kinetic energy, k_{res}. This ratio is a function of time, t, and space, $\boldsymbol{x}$. As a recommendation, Pope [1] suggests that when $M \lesssim 0.2$, a simulation is sufficiently well resolved. Physically, this assumes that 20% of the turbulent kinetic energy contained in the SGSs does not significantly affect the flow solution. Although the definition of M is straightforward, directly evaluating the SGS turbulent kinetic energy may not be trivial and has to be approximated. Pope's criterion has been applied to a variety of flow-field simulations, such as nonreacting flows [5], gas turbine combustion chambers [6,7], and cardiovascular flows [8]. All of these studies used $M \lesssim 0.2$ as an indicator of satisfactory quality of the solution.

Another method for assessing the quality of a simulation from statistical flow-field results is the Index of Resolution Quality (IQ) for LES [2], which reads

$$\mathrm{LES_{IQ}} = \frac{k_{\mathrm{res}}}{k_{\mathrm{tot}}}. \tag{2}$$

Similarly to Pope's criterion, this index compares the resolved turbulent kinetic energy and the total turbulent kinetic energy, k_{tot}. Here the residual scales are approximated using Richardson extrapolation as $k_{\mathrm{tot}} - k_{\mathrm{res}} = a_k h^p$, where h is the grid size (typically assumed to be equal to the filter width, Δ), p is the order of accuracy, and a_k is a coefficient that is determined by running the simulation on two different sized grids. Values of $\mathrm{LES_{IQ}}$ between 0.75 and 0.85 are considered adequate for engineering applications [2,9].

Another metric considers the velocity field [3,10],

$$M_v = \frac{T_{\mathrm{sgs}}}{T_{\mathrm{res}} + T_{\mathrm{sgs}}}, \tag{3}$$

which compares the SGS velocity fluctuations, T_{sgs}, to the sum of the resolved velocity fluctuations, T_{res}, and the SGS velocity fluctuations. As in $\mathrm{LES_{IQ}}$, this index asymptotically approaches zero as the simulation approaches the DNS limit, and unity as the simulation approaches the RANS limit.

Similarly to a velocity-statistics metric, the ratio of the turbulent viscosity to the molecular viscosity can also be used to determine the LES quality [10,11]. In regions where this ratio is very large, further refinement is likely necessary due to a high percentage of the viscosity being modeled. In regions where there is no turbulence, this ratio should be zero. As a LES is refined, the turbulent viscosity decreases until the limit of DNS, for which the ratio tends to zero.

Although these statistical metrics are practical, LES is inherently unsteady, and a dynamic measure is desirable to further characterize the LES quality in representing the dynamic content of a simulation. This is particularly relevant for flows that are inherently transient. The key observation is that turbulence is a deterministic chaotic phenomenon, which is characterized by an aperiodic long-term behavior exhibiting high sensitivity to the initial conditions. Different approaches exist to measure and characterize a chaotic solution [12–16]. On one hand, geometric approaches estimate the fractal dimension of the chaotic attractor, which, in turn, gives an estimate of the active degrees of freedom of the chaotic dynamical system. An accurate measure is the Hausdorff dimension [13], which is often approximated by box counting, based on phase-space partitioning and correlation dimension based on time series analysis [15]. On the other hand, dynamical approaches estimate the entropy content of the solution, namely, the frequency with which a solution visits different regions of an attractor, for example, by the Kolmogorov-Sinai entropy, and the separation of two close solutions via the Lyapunov exponents. In turbulence, these measures of chaos have been applied to simple inert flow configurations [16]. In particular, the maximal Lyapunov exponent, λ, is relatively straightforward to calculate and amenable to a simple physical explanation: If a system is chaotic, given an infinitesimal initial perturbation to the solution, two trajectories of the system separate in time exponentially until nonlinear saturation. The average exponential separation is the Lyapunov exponent. A solution is typically regarded as being chaotic if there exists at least one positive Lyapunov exponent. The Lyapunov exponent is (1) a robust indicator of chaos, (2) a global quantity describing the strange attractors—the attractors of chaotic solutions—because it does not depend on the initial conditions for ergodic processes [17], and (3) relatively simple to calculate [16,18–21]. In addition, there are several benefits of using this method over the traditional Pope's criterion. First, the Lyapunov exponent can be used on transient simulations where a statistically stationary flow is not present and the ability to determine the resolved and unresolved turbulence fluctuations may not be possible. Second, calculating the Lyapunov exponent can be accomplished quickly for arbitrary meshes or geometries and is independent of any closure models. Finally, using the analysis of the Lyapunov exponent additional information on local turbulence and sensitivity to domain size and shape can be obtained. For these reasons, the first objective of this paper is to propose the Lyapunov exponent as a metric to evaluate the quality of LES in describing the short-time dynamics of the turbulent flow.

The Lyapunov exponent represents the rate of separation, and its reciprocal is closely related to the predictability horizon of a chaotic solution. Turbulent flows, which are governed by partial differential equations, do not completely lack predictability because they are deterministic systems. The phase space is infinite-dimensional; however, the strange attractor is finite-dimensional. Its fractal dimension corresponds to the finite number of "unpredictable" features [22,23]. For infinitesimal perturbations in inert flows, the Lyapunov exponent should scale as the inverse of the shortest time scale, which is the Kolmogorov time scale, τ_η. In other words, $\lambda \sim \tau_\eta^{-1} \sim \mathrm{Re}^\alpha$, where $\alpha = 1/2$ from Kolmogorov theory [12], whereas $\alpha \approx 0.46$ in a multifractal approach [24]. The discrepancy between these two values is due to the intermittency of the cascade [20,25,26]. At larger scales, from phenomenological arguments, the predictability time is often related to the turnover time of the energy containing eddies [27,28].

Determining the predictability horizon of simulations is of importance for various practical applications. With the increase in computational power, the ability to use high-fidelity simulations as a tool for real-time predictions and forecasting may soon be possible. For this type of application, it is important to understand the time scales at which the simulation diverges from the true solution, given a finite accuracy of the boundary and initial conditions. So far, the predictability of turbulent flows has been investigated in simple configurations, such as two-dimenisonal turbulence; however, the effect of combustion has not been investigated yet. Therefore, the second objective of this paper is to evaluate the effect that combustion has on the predictability of turbulent jets. The Lyapunov exponent as a dynamic quality index for LES is examined by considering two different turbulent configurations. First, forced homogeneous isotropic turbulence (FHIT), which represents a well-characterized turbulent flow of academic interest, is selected. The second configuration consists of a turbulent jet flame, in which the turbulent combustion is represented using a manifold-based combustion model. Results from this simulation will be compared against an inert jet-flow simulation that is performed at the same nozzle-exit conditions, thereby establishing a direct assessment of the combustion process on the turbulence dynamics through the Lyapunov metric.

The rest of this paper is organized as follows. The theory and practical evaluation of the Lyapunov exponent in DNS and LES calculations are discussed in Secs. II and III. In the FHIT configuration in Sec. IV, various tests and results for different filter widths, initial perturbation fields, and perturbation magnitudes are presented. In the jet configuration in Sec. V, the convergence of the Lyapunov exponents for different grids of varying resolution and spatial extend is examined. The effect of combustion is investigated by comparing the predictability of the reacting jet with the corresponding inert case. The paper ends with concluding remarks in Sec. VI.

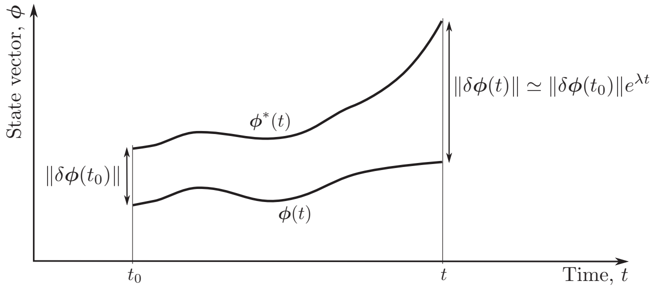

FIG. 1. Separation of two slightly different solutions. The initial divergence is exponential, and the growth rate is the Lyapunov exponent, λ.

II. LYAPUNOV EXPONENT

A. Dynamical system representation

A turbulent flow can be represented as a dynamical system,

$$\dot{\boldsymbol{\phi}}(t) = \mathbf{F}(\boldsymbol{\phi}(t)), \tag{4}$$

with initial conditions $\boldsymbol{\phi}(t = t_0) = \boldsymbol{\phi}_0$; $\mathbf{F}$ is the set of bounded differentiable flow equations, and $\dot{\boldsymbol{\phi}}$ denotes the temporal derivative of the state vector $\boldsymbol{\phi}$. For a general chemically reacting flow, $\boldsymbol{\phi}$ contains the velocity vector ($\boldsymbol{u}$), pressure (p), density (ρ), and vector of species mass fractions ($\boldsymbol{Y}$): $\boldsymbol{\phi} = (\boldsymbol{u},p,\rho,\boldsymbol{Y})^T$. The solution $\boldsymbol{\phi}(t)$ belongs to a vector space H, called the phase space. In the finite-dimensional case, $H = \mathbb{R}^N$, where $N \in \mathbb{N}$. In the infinite-dimensional case H is a Hilbert space. The fluid dynamics problems studied are infinite-dimensional because they are governed by PDEs. However, they are characterized by the existence of a bounded set, called the strange attractor, because they are dissipative systems. This means that the turbulent solution lies in a fractal set with finite dimension [29]. Moreover, after numerical discretization, the phase space necessarily becomes finite-dimensional. Hence, the fluid systems are considered finite-dimensional in this paper.

Consider two initial conditions $\boldsymbol{\phi}_0$ and $\boldsymbol{\phi}_0^*$, which are infinitesimally distanced, $\boldsymbol{\phi}_0^* - \boldsymbol{\phi}_0 = \delta\boldsymbol{\phi}_0$ (see Fig. 1 for a schematic illustration). The temporal evolution of the separation of the two trajectories, $\delta\boldsymbol{\phi}(t)$, in the tangent space obeys the linearized dynamical equation $\delta\dot{\phi}_i(t) = \sum_{j=1}^{N_D} \frac{\partial F_i}{\partial \phi_j}\delta\phi_j(t_0)$, where $i = 1,2,\ldots,N_D$, with N_D being the number of degrees of freedom of the system, i.e., the dimension of the phase space. In the present study, $N_D \sim O(10^7)$ for most cases.

Under ergodicity, Oseledets [30] proved that there exists an orthonormal basis $\{\mathbf{e}_j\}$ in the tangent space such that the solution can be expressed by a modal expansion, $\delta\boldsymbol{\phi}(t) = \sum_{j=1}^{N_D} \alpha_j \mathbf{e}_j e^{\lambda_j t}$, where the coefficients α_j depend on the initial condition $\delta\boldsymbol{\phi}(t_0)$. Mathematically, $\alpha_j = \langle \mathbf{e}_j,\delta\boldsymbol{\phi}(t_0)\rangle$, where the angular brackets denote an inner product. The exponents $\lambda_1 \geqslant \lambda_2 \geqslant \cdots \geqslant \lambda_{N_D}$ are the Lyapunov exponents. Customarily, the maximal Lyapunov exponent, λ_1, is referred to as Lyapunov exponent, and the subscript is omitted ($\lambda \equiv \lambda_1$). In the phase space, the modal expansion describes the deformation of an N_D-dimensional sphere of radius $\delta\boldsymbol{\phi}(t_0)$ centered at $\boldsymbol{\phi}(t_0)$ into an ellipsoid with semiaxes along the directions $\mathbf{e}_j$. Therefore, the Lyapunov exponents provide the stretching rates along these principal directions. Thus, given an infinitesimal initial perturbation to the solution, $\delta\boldsymbol{\phi}(t_0)$, the two trajectories of the system separate in time exponentially as [16]

$$\|\delta\boldsymbol{\phi}(t)\| \simeq \|\delta\boldsymbol{\phi}(t_0)\|e^{\lambda t}, \tag{5}$$

where $\|\cdot\|$ is a norm. Figure 1 illustrates the significance of the Lyapunov exponent. The predictability time, t_p, of the system for infinitesimal perturbations is then defined as the inverse of

TABLE I. Algorithm 1: Procedure for the evaluation of the Lyapunov exponent.

```
1: Run numerical simulation until statistical convergence of the solution $\boldsymbol{\phi}$ is reached
2: Reset time to $t = t_0$ and save solution $\boldsymbol{\phi}$
3: At time $t = t_0$ compute $\boldsymbol{\phi}^*$ by perturbing the solution $\boldsymbol{\phi}$ following Eq. (7)
4: Advance both solutions, $\boldsymbol{\phi}$ and $\boldsymbol{\phi}^*$, to some time $t$
5: Calculate the norm of the separation field $\delta\boldsymbol{\phi}$ from Eq. (8)
6: Take logarithm of separation norm, $\log_{10}(\|\delta\boldsymbol{\phi}\|)$ and calculate the Lyapunov exponent, $\lambda$, as slope of the linear region using linear regression
7: Normalize separation norm with saturation value to simplify inspection
```

the Lyapunov exponent

$$t_p = \ln\left[\frac{\|\delta\boldsymbol{\phi}(t)\|}{\|\delta\boldsymbol{\phi}(t_0)\|}\right]\frac{1}{\lambda} \sim \frac{1}{\lambda}, \tag{6}$$

which is physically the time that a small separation, $\delta\boldsymbol{\phi}(t_0)$, takes to get amplified by approximately a factor of 2.7.

B. Calculation of the Lyapunov exponent as a separation growth rate

The objective now is to utilize the Lyapunov exponent as an estimate for the rate of divergence of the Eulerian solution obtained by LES. From this information, a metric is proposed to measure how dynamically well resolved the turbulent solution is. Using the Eulerian solution is a natural choice since most numerical simulations calculate Eulerian quantities. Growth rates of Eulerian fields have been used before in evaluating the error growth of weather models [18,21], finite perturbations of fully developed turbulence [20], and decaying two-dimensional turbulence [19]. By observing that an Eulerian field can be regarded as a trajectory in an extended dynamical system [20], a practical method for obtaining the Lyapunov exponent is to perturb the initial field $\boldsymbol{\phi}(t_0)$ as

$$\boldsymbol{\phi}^*(t_0) = \boldsymbol{\phi}(t_0) + \epsilon\|\boldsymbol{\phi}(t_0)\|, \tag{7}$$

where $\epsilon \ll 1$, $\|\cdot\| \equiv [\frac{1}{V}\int_V (\cdot]^p dV)^{1/p}$ is the L_p-norm, and V is the volume of the domain. The separation, also known as *error* [21], is then measured by the L_p-norm of the subtracted Eulerian fields,

$$\|\delta\boldsymbol{\phi}\| = \|\boldsymbol{\phi}^*(t) - \boldsymbol{\phi}(t)\|. \tag{8}$$

The separation behaves in accordance to Eq. (5), thus, the Lyapunov exponent is computed as the linear slope of the natural logarithm of the separation versus time, $\lambda t = \ln(\|\delta\boldsymbol{\phi}(t)\|/\|\delta\boldsymbol{\phi}(t_0)\|)$. In the remainder of this paper, the L_2-norm is chosen to measure the separation in Eq. (8).

If the process is ergodic, as assumed in this paper, the Lyapunov exponent is independent of the initial conditions as long as the nearly infinitesimal limit is satisfied [12,30].

The procedure for calculating the Lyapunov exponent is given in Table I.

C. Lyapunov metric for LES

Compared to LES-quality metrics that rely on statistical information about turbulent kinetic energy or other flow-field quantities, the Lyapunov exponent intrinsically depends on the dynamic and chaotic nature of turbulence. While many turbulent flow systems in engineering are able to be time-averaged, some systems involve highly dynamic flows that cannot be averaged. For example, rare events are particularly difficult to simulate and capture, such as preignition, extinction, or cycle-to-cycle variations in internal combustion engines. These rare events happen on a very small time scale, therefore, the simulations of these systems must be able to resolve the relevant dynamic scales to attempt to simulate these phenomena. As shown subsequently, the Lyapunov exponent saturates when the dynamical scales of the problem saturate. Specifically, as the spatio-temporal resolution approaches the smallest physical scales, the magnitude of the Lyapunov exponent reaches a plateau. This, in turn, provides a robust evaluation of the resolution requirements and spatial dimension of the computational domain in LES to capture the fundamental turbulent dynamics of rare deterministic events.

One caveat in using the Lyapunov exponent is that its asymptotic value is not known *a priori*; current results show that the Lyapunov time scale scales with the integral time scale for both the FHIT and jet cases. Iteration of resolution is likely required for more complex geometries and physics. The Lyapunov exponent is expected to be dependent on physical models and numerical discretization and can therefore be used as a sensitivity parameter and indicator to characterize their quality.

III. GOVERNING EQUATIONS

The evolution of the turbulent flow in LES is governed by the Favre-filtered form of the Navier-Stokes equations. The Favre-filtered quantity of a scalar ψ is computed as

$$\widetilde{\psi}(t,\boldsymbol{x}) = \frac{1}{\overline{\rho}} \int \rho(t,\boldsymbol{x}')\psi(t,\boldsymbol{x}')G(\boldsymbol{x},\boldsymbol{x}';\Delta)\,d\boldsymbol{x}', \tag{9}$$

where G is the filter kernel. The residual field is then evaluated as $\psi'' = \psi - \widetilde{\psi}$, and a Favre-filtered quantity is related to a Reynolds-filtered quantity by $\overline{\rho}\widetilde{\psi} = \overline{\rho\psi}$. With this, the filtered conservation equations for mass, momentum, and scalar transport, describing a chemically reacting flow in the low-Mach number limit, take the following form:

$$\partial_t\overline{\rho} + \partial_j(\overline{\rho}\widetilde{u}_j) = 0, \tag{10a}$$

$$\partial_t(\overline{\rho}\widetilde{u}_i) + \partial_j(\overline{\rho}\widetilde{u}_j\widetilde{u}_i) = -\partial_i\overline{p} + \partial_j\overline{\sigma}_{ij} + \partial_j\tau_{ij}^{\text{sgs}} + f_i, \tag{10b}$$

$$\partial_t(\overline{\rho}\widetilde{\psi}) + \partial_j(\overline{\rho}\widetilde{u}_j\widetilde{\psi}) = \partial_j(\overline{\rho}\widetilde{\alpha}_\psi\partial_j\widetilde{\psi}) + \partial_j\tau_{\psi j}^{\text{sgs}} + \overline{\rho}\widetilde{\omega}_\psi, \tag{10c}$$

where $\partial_j \equiv \partial/\partial x_j$, $\widetilde{u}_i$ is the ith filtered velocity component, $\overline{p}$ is the filtered pressure, $\overline{\rho}$ is the filtered density, $\widetilde{\alpha}_\psi$ is the mass diffusivity of scalar ψ, f_i is a forcing term, and $\widetilde{\omega}_\psi$ is the filtered chemical source term. The filtered viscous stress tensor is

$$\overline{\sigma}_{ij} = 2\overline{\mu}\big(\widetilde{S}_{ij} - \tfrac{1}{3}\partial_k\widetilde{u}_k\delta_{ij}\big) \quad \text{with} \quad \widetilde{S}_{ij} = \tfrac{1}{2}(\partial_i\widetilde{u}_j + \partial_j\widetilde{u}_i), \tag{11}$$

and the Reynolds stress tensor, τ_{ij}^{sgs}, is modeled by a turbulent viscosity formulation,

$$\tau_{ij}^{\text{sgs}} = 2\mu_T\widetilde{S}_{ij} - \tfrac{2}{3}\rho\widetilde{k}\delta_{ij} \quad \text{where} \quad \mu_T = \overline{\rho}C_s\Delta^2(2\widetilde{S}_{ij}\widetilde{S}_{ij})^{1/2}, \tag{12}$$

and the Germano model [31] is employed to evaluate C_s.

In the following, we consider two turbulent flow configurations: the inert forced homogeneous isotropic turbulence and a turbulent jet flame. For the case of an inert flow, the density and viscous-diffusive transport properties are constant, so that these inert flows are fully described by the solution of Eqs. (10a) and (10b). In contrast, the representation of the reacting flows requires the consideration of the variable thermo-viscous-diffusive quantities on the combustion. For this, a reaction-diffusion manifold combustion model is employed [32,33], in which these quantities are expressed in terms of a reduced manifold model that is parameterized in terms of the mixture fraction, Z, and a reaction progress variable, C. With this, the scalar solution vector in Eq. (10c) becomes $\boldsymbol{\psi} = (Z,C)^T$, and C is evaluated as the sum of major product mass fractions. In the present study, the reaction-diffusion manifold is obtained from the solution of steady flamelet equations, and a presumed probability density function (PDF) is used to account for the turbulence and chemistry interaction. Denoting all thermo-chemical properties by $\boldsymbol{\xi}$, the filtered quantities are then parameterized by the state equation $\widetilde{\boldsymbol{\xi}} = \widetilde{\boldsymbol{\xi}}(\widetilde{Z},\widetilde{Z''^2},\widetilde{C})$, which introduces the mixture fraction variance, $\widetilde{Z''^2}$, that is here evaluated from an algebraic model [34]. A detailed description of the combustion model and application to the jet flame under investigation can be found in Refs. [35–37].

Statistical quantities are evaluated from the turbulent flow simulations by averaging over homogeneous directions and time. Hence, a Favre-averaged mean-flow quantity is denoted by $\langle\widetilde{\phi}\rangle$ and the resolved fluctuation is $\widetilde{\phi}''_<$ so that $\widetilde{\phi} = \langle\widetilde{\phi}\rangle + \widetilde{\phi}''_<$. The resolved turbulent kinetic energy is then computed as $k_{\text{res}} = \frac{1}{2}\langle\widetilde{u}''_{i<}\widetilde{u}''_{i<}\rangle$, and the SGS turbulent kinetic energy is approximated as $k_{\text{sgs}} = \langle\nu_T^2/(C_s\Delta^2)\rangle$, where $\nu_T = \mu_T/\overline{\rho}$ is the kinematic turbulent viscosity, and Δ is the filter width, which is the cube root of the volume of a cell.

IV. FORCED HOMOGENEOUS ISOTROPIC TURBULENCE

This section examines the Lyapunov exponent and predictability for forced homogeneous isotropic turbulence [38–40] by DNS and LES. In particular, effects of perturbation magnitude, mesh refinement, and convergence of the Lyapunov exponent are examined.

A. Model and computational setup

Homogeneous incompressible isotropic turbulence is simulated on a $(2\pi)^3$ periodic Cartesian domain (units are self-consistent). The velocity components are denoted as $\widetilde{\boldsymbol{u}} = (\widetilde{u},\widetilde{v},\widetilde{w})^T$, and the problem is fully described by conservation equations for mass and momentum, Eqs. (10a) and (10b), in which density and viscosity are constant so that the continuity equations reduces to the divergence-free velocity condition, $\partial_j\widetilde{u}_j = 0$.

The simulations are initialized with a von Karman-Pao spectrum using turbulence values similar to target values. The initial conditions were set to a turbulent Reynolds number of $\text{Re}_T = 300$, the ratio of integral length scale to the size of the computational domain is $\ell/\mathcal{L} = 0.3226$, and the ratio of Kolmogorov length scale to the mesh size is $\eta/\Delta = 1.15$. Here the integral length scale is given by $\ell = k^{3/2}/\varepsilon$, the Kolmogorov length scale is $\eta = (\nu/\varepsilon)^{1/2}$, and $\text{Re}_T = k^2/(\varepsilon\nu)$.

A linear forcing term, $f_i = A\widetilde{u}_i$ is added to the right-hand side of Eq. (10b) to obtain statistically stationary turbulence [41]. The resolved turbulent kinetic energy equation is

$$\partial_t k_{\text{res}} = -\varepsilon_{\text{res}} - \varepsilon_{\text{sgs}} + 2Ak_{\text{res}}, \tag{13}$$

where ε_{res} is the resolved viscous dissipation, ε_{sgs} is the SGS viscous dissipation, and ν is the kinematic viscosity. In order to compare the LES cases, the total turbulent kinetic energy and dissipation are evaluated from the resolved and SGS contributions: $k \approx k_{\text{res}} + k_{\text{sgs}}$ and $\varepsilon \approx \varepsilon_{\text{res}} + \varepsilon_{\text{sgs}}$.

To ensure stationary turbulence, Eq. (13) is set to zero. Given a target resolved turbulent kinetic energy, k_{res}, and total viscous dissipation, ε, the forcing amplitude, A, is given by $A = \varepsilon/2k_{\text{res}}$ [41].

As noted in Ref. [38], a constant forcing coefficient prescribes an eddy turnover time scale but has no set length scale, so the simulation will adjust accordingly as the solution advances. The solution is advanced in time until it reaches a statistically stationary state for the turbulent kinetic energy and dissipation with a target turbulence Reynolds number of 300. Since the forcing is applied to the resolved scales in the LES cases, iteration of the forcing coefficient is required for the coarser cases because the SGS turbulent kinetic energy is used to calculate the turbulent quantities of interest. The typical time to reach this state is around 20 eddy turnover times. The variance in turbulent kinetic energy and dissipation is of the order of 10% [41]. Based on the results of Ref. [42], the normalized Lyapunov exponent is not expected to significantly change with these variances.

B. DNS analysis: Effect of perturbation

To examine the effect of initial perturbations on the Lyapunov exponent, we begin our study by considering DNS, in which all scales are resolved and the turbulent viscosity and SGS dissipation become zero. Because the flow configuration is in principle an infinite-dimensional dynamical system, the Lyapunov exponents could depend on the type of initial perturbations [16]. Therefore, a number of perturbations and initial conditions are tested to determine the robustness of the Lyapunov exponent. For this, we consider the magnitude of the perturbation ϵ in Eq. (7) and the quantity that is perturbed. The different types of perturbations considered in this study are summarized in Table II.

TABLE II. Effect of initial perturbations and perturbed variables on Lyapunov exponent.

$\log_{10}(\epsilon)$	Perturbed variable(s)	$\lambda\tau_\eta$
-8	u,v,w	0.114
-4	u	0.115
-6	u	0.116
-8	u	0.117
-10	u	0.116

In the first test, all three velocity components (u,v,w) are perturbed by a value of $\epsilon = 10^{-8}$ using Eq. (7). The temporal evolution of the separation is shown in Fig. 2. The time is nondimensionalized by the Kolmogorov time scale, $\tau_\eta = (\nu/\varepsilon)^{1/2}$. All of the variable separations grow uniformly and homogeneously in time. Although the system is high-dimensional, the separation exhibits behavior similar to traditional low-dimensional chaotic systems such as the Lorenz model [43]. Three distinct regions can be identified (Fig. 2): an initial response, a linear region, and a region of saturation. The velocity fields diverge initially from small structures to larger homogeneous isotropic structures over time.

The Lyapunov exponent is evaluated from the slope of the separation in the logarithmic region following Eq. (5). The slope of this region is determined by maximizing the correlation coefficient given a desired linear fit size across the region. As noted in Sec. II A, the inverse of this exponent is related to the predictability time with an initial and desired error. The normalized Lyapunov exponent for this case is $\lambda\tau_\eta = 0.114$, which corresponds to a predictability time of $t_p \approx 1/\lambda \approx 9\tau_\eta$. The ratio of the eddy turnover time, $\tau_\ell = k/\varepsilon$, to Kolmogorov time, τ_η, is $\tau_\ell/\tau_\eta = \sqrt{\mathrm{Re}_T} \approx 17$. The Lyapunov time falls between these two time scales for this problem. The implication of this analysis is that no matter how accurate the initial conditions are for this system, given the fact that

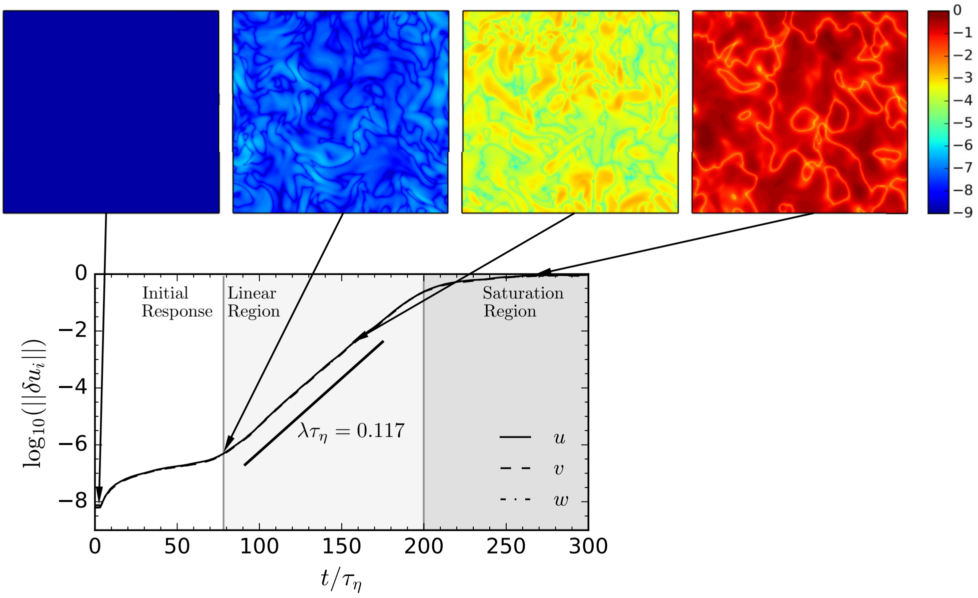

FIG. 2. Separation and Lyapunov exponent for the FHIT DNS with time normalized by the Kolmogorov time scale, τ_η. The contours correspond to the absolute values of the difference of u between two separated simulations. The three distinct regions are separated by both vertical lines and different backgrounds.

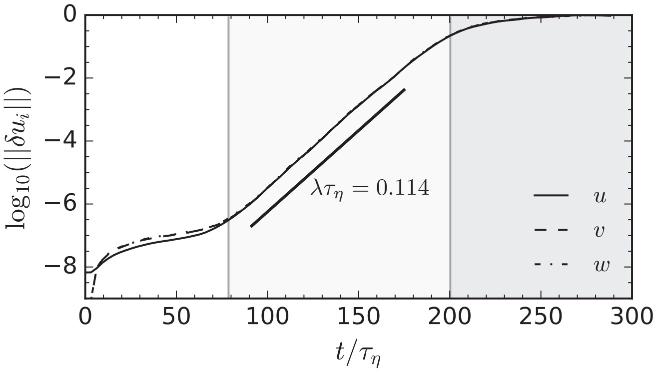

FIG. 3. Separation as a function of time for initial perturbations to u with $\epsilon = 10^{-8}$. The three distinct regions are separated in the same way as Fig. 2.

numerical simulations are not infinitely precise, the simulated turbulent velocity field will diverge in a few eddy turnover times; the predictability time and Lyapunov exponent provide quantitative information about the time horizon over which a turbulent event can be simulated. Saturation occurs in this case because the separation cannot grow further than the average fields as the simulation becomes statistically stationary.

In the next step, only one component of the velocity vector, u, is perturbed initially with a perturbation magnitude of $\epsilon = 10^{-8}$. The evolution of the separation distance for all three velocity components is shown in Fig. 3. The initial response region for the nonperturbed variables are slightly different since they evolve from the initially unperturbed field due to nonlinear coupling through the governing equations. However, it can be seen that after this initial response phase, the separation becomes indistinguishable between all three velocity components.

The last aspect to investigate is the effect of the perturbation magnitude on the evolution of the separation and the Lyapunov exponent. For this, the magnitude of the initial perturbation is varied over the following range: $\epsilon = \{10^{-4}, 10^{-6}, 10^{-8}, 10^{-10}\}$, and only the u-velocity component is perturbed. Results from this investigation are presented in Fig. 4. Since the Lyapunov exponent theoretically does not depend on the initial condition [30], a smaller perturbation extends the linear region and a larger perturbation shrinks the linear region while maintaining the same slope. The initial-response region for all cases remains approximately the same, and for these reasons the saturation occurs earlier for larger perturbations. By evaluating the Lyapunov exponent for all

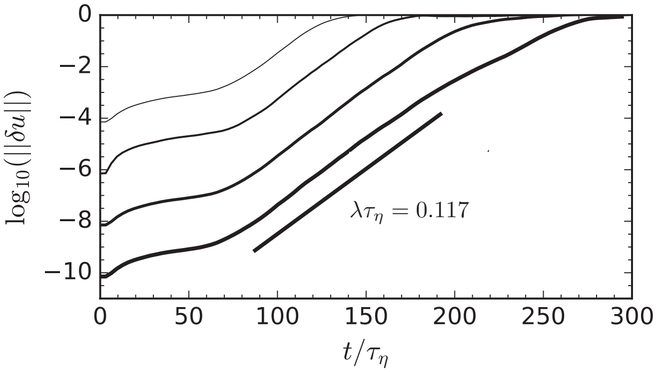

FIG. 4. Separation as a function of time for initial perturbations to the u-velocity component for $\epsilon = \{10^{-4}, 10^{-6}, 10^{-8}, 10^{-10}\}$ (from top to bottom).

TABLE III. Test cases for FHIT. N is the number of grid points in one direction, A is the forcing coefficient, Re_T is the turbulence Reynolds number, $\mathcal{L}/\ell$ is the ratio of the size of the domain to the integral length scale, Δ/η is the ratio of the filter width to the Kolmogorov scale, M is Pope's criterion, ν_T/ν is the ratio of turbulent to molecular viscosity, and $\lambda\tau_\eta$ is the normalized Lyapunov exponent. There are fluctuations in both turbulent kinetic energy and dissipation of around 10%, which is the reason for the small discrepancies in cases d through f.

Case	N	$A\tau_\ell$	Re_T	$\mathcal{L}/\ell$	Δ/η	M	ν_T/ν	$\lambda\tau_\eta$
a	16	0.488	336 ± 51	2.49	12.23	3.1×10^{-2}	1.5×10^{0}	0.063
b	32	0.525	353 ± 59	2.49	6.33	1.3×10^{-2}	4.3×10^{-1}	0.074
c	64	0.559	302 ± 42	2.65	3.00	2.9×10^{-3}	7.0×10^{-2}	0.078
d	128	0.575	400 ± 60	2.60	1.82	4.1×10^{-4}	1.0×10^{-2}	0.129
e	216	0.533	336 ± 6	2.72	0.99	1.0×10^{-5}	2.4×10^{-4}	0.115
f	256	0.533	333 ± 30	2.73	0.83	1.3×10^{-7}	3.0×10^{-6}	0.123
f_{DNS}	256	0.543	300 ± 10	3.10	0.87	0	0	0.114

four cases, it is confirmed that λ is virtually invariant to the initial conditions, provided that the perturbation is sufficiently small.

C. LES analysis: Effect of grid refinement

The quality of an LES solution depends on the accuracy of the SGS models and numerical resolution that contribute to the dynamics of the turbulent flow. To examine the effect of the resolution on the dynamics that is characterized by the Lyapunov exponent, a series of LES computations are performed. The individual test cases under consideration together with relevant parameters are summarized in Table III. In this study, only the u-velocity is perturbed by $\epsilon = 10^{-8}$, and the effect of the grid refinement is investigated.

The resolved energy spectra are shown in Fig. 5. This comparison shows that as the resolution is increased, the dissipative end of the spectrum grows as expected. The inertial subrange proportional to $k^{-5/3}$ is present for all seven cases. The spectra do not exhibit a large inertial subrange due to the relatively low turbulence Reynolds number.

The temporal evolution of the computed separation is shown in Fig. 6. From this figure, it can be seen that the initial response region enlarges both in magnitude and time as the grid is refined up to $N = 128$ (case d). The same fast-response region is observed in the accompanying DNS case (case f_{DNS}), which leads to the conclusion that the effect is independent of the LES method. Importantly, these results show that the Lyapunov exponent monotonically

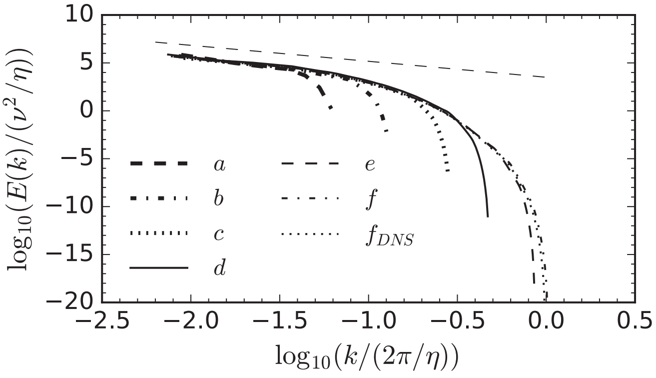

FIG. 5. Energy spectra for all LES cases summarized in Table III.

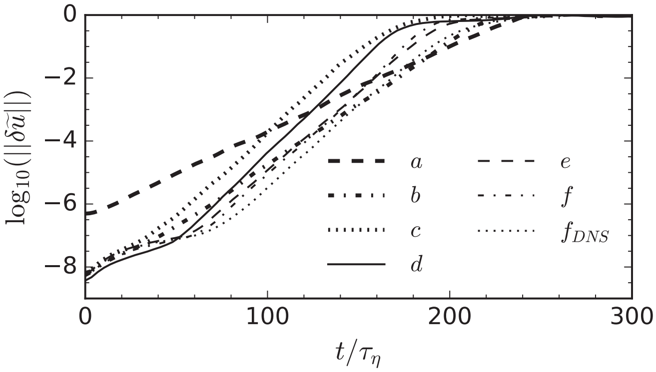

FIG. 6. Separation and Lyapunov exponents as a function of grid resolution. The Lyapunov exponent and initial-response region increase as the grid is refined up to $N = 128$. Note that the initial-response region depends on the initial condition.

increases with decreasing filter width to a plateau around $\lambda\tau_\eta = 0.12$. Physically, the Lyapunov exponent is a global chaotic parameter. Consequently, it is expected that the Lyapunov exponent saturates when the smallest dynamic and chaotic scales are resolved, and this is confirmed in Table III.

A summary of the computed Lyapunov exponents as a function of the filter size is shown in Fig. 7. As the grid size approaches the Kolmogorov scale, the Lyapunov exponent of the system is approaching a plateau. This plateau is indicative that the degrees of freedom contributing to the global chaotic dynamics are fully resolved. According to the Kolmogorov scale, an oversampled grid yields the same chaotic dynamics as a grid spacing of the size of the Kolmogorov scale (Table III). This analysis shows that for case d with 128^3 grid points, the Lyapunov exponent saturates. This implies that $\eta/\Delta = 0.55$ is sufficient to capture the smallest chaotic dynamical scales and all the relevant active degrees of freedom for this system. This saturation of the Lyapunov exponent is therefore a way to characterize DNS resolution. Previous studies [44] find that a ratio of $\eta/\Delta = 0.34$ or better indicates a quality DNS. The results compare favorably and show that the grid for a numerical DNS should be around two to three times the Kolmogorov scale.

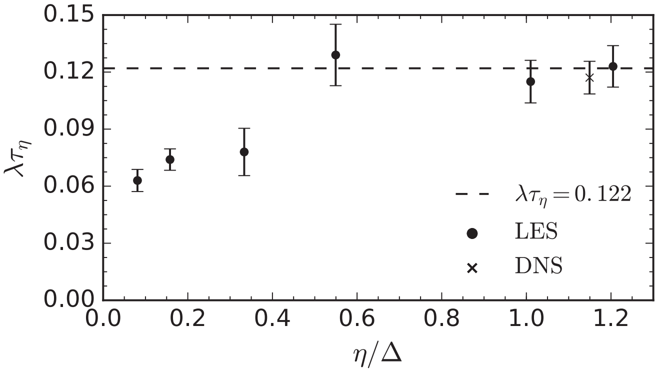

FIG. 7. Normalized Lyapunov exponent as a function of the ratio between Kolmogorov scale and LES filter width. Error bars take into account a 5% error due to Reynolds number fluctuations [42] and an additional error in the Kolmogorov time scale due to fluctuations. The Lyapunov exponent tends to a plateau, $\lambda\tau_\eta \approx 0.122$, in case d. For this case, 99.96% of the turbulent kinetic energy is resolved.

TABLE IV. Mesh resolution of the five different grids used.

Grid	N_x	N_r	N_θ
1	80	40	16
2	160	80	32
3	320	160	64
4	640	320	128
5	960	480	128

V. TURBULENT JETS

In this section, the analysis of the Lyapunov exponent is extended and applied to a turbulent jet flow. To gain fundamental understanding about the effect of combustion on the flow dynamics, studies of reacting and inert jets are performed.

A. Model and computational setup

Large-eddy simulations of inert and reacting turbulent jets are performed. The operating conditions for the inert jet are chosen for comparison with experimental data [45]. In this experiment, the jet is exiting from a pipe, and the length of the pipe is sufficiently long to ensure that the flow is fully developed when the fluid exits the nozzle. The jet-exit Reynolds number in this experiment is $\mathrm{Re} = 16\,000$, and the passive scalar is represented by heating the fluid, which exits the nozzle.

A nonpremixed jet flame configuration at similar operating conditions was studied experimentally [46–48]. The burner configuration consists of a central fuel nozzle of diameter $D_{\mathrm{ref}} = 8$ mm, surrounded by a coflow nozzle of square shape. The jet fluid consists of a mixture of 22.1% CH_4, 33.2%H_2, and 44.7%N_2 by volume with a stoichiometric mixture fraction of $Z_{\mathrm{st}} = 0.167$. The fuel bulk velocity is $U_{\mathrm{ref}} = 42.2$ m/s. Coflowing air is supplied at an axial velocity of $7.11\times10^{-3}U_{\mathrm{ref}}$. The jet-exit Reynolds number is $\mathrm{Re} = 14\,720$. In the following, all quantities are nondimensionalized appropriately using U_{ref} and D_{ref}, and conditions of the jet flow.

Combustion is modeled by the flamelet or progress variable (FPV) approach [32,33]. In this combustion model, all thermochemical quantities are parameterized by a three-dimensional reaction-diffusion manifold. For all reactive flow simulations, the reaction chemistry is described by the GRI 2.11 mechanism [49], consisting of 279 reactions among 49 species. The governing equations, given in Eqs. (10), are solved on a cylindrical coordinate system $\boldsymbol{x} = (x,r,\varphi)^T$. The computational domain is $120D_{\mathrm{ref}}\times45D_{\mathrm{ref}}\times2\pi$ in axial, radial, and azimuthal directions, respectively. A well-resolved LES pipe flow using the jet parameters is first simulated to obtain the inflow conditions for the flame. Convective outflow conditions are used at the outlet and no-slip boundary conditions are employed at the lateral boundaries. The domain is initialized with the coflow velocity and then advanced in time using a CFL number of approximately 0.5. Once the inert jet reaches a statistically stationary state, the combustion model is turned on and the jet is advanced in time until it is statistically stationary. Large-eddy simulations of five grids, shown in Table IV and Fig. 8, are simulated.

The mesh resolution should be compared with the Kolmogorov length scale, η. This scale can be reasonably well estimated as [50]: $\eta = (\mathrm{Re}^3\,\varepsilon)^{-1/4}$ with $\varepsilon = \xi u'^3/\ell$, $\xi \approx 0.33$, $\ell \approx 0.226 r^u_{1/2}$. The integral length scale is ℓ, u' is the root-mean-square velocity, ε is the dissipation rate, and $r^u_{1/2}$ is the jet half width. The Kolmogorov length scales for both cases are evaluated at a location near the nozzle lip, with $r^u_{1/2} = 1/2$, and $u' = 0.2$. At this location the kinematic viscosity increases due to heat release for the reactive jet, resulting in a local Reynolds number based on jet diameter and jet exit velocity of $\mathrm{Re}_{1/2} = 1800$ for the reacting jet. The estimated length scales are summarized in Table V. At the finest grid spacing, the grid size is on the order of the Kolmogorov scale.

Each solution is advanced in time until it is statistically stationary. Statistics are obtained by averaging over the azimuthal direction and in time, and results for mean and root-mean-square

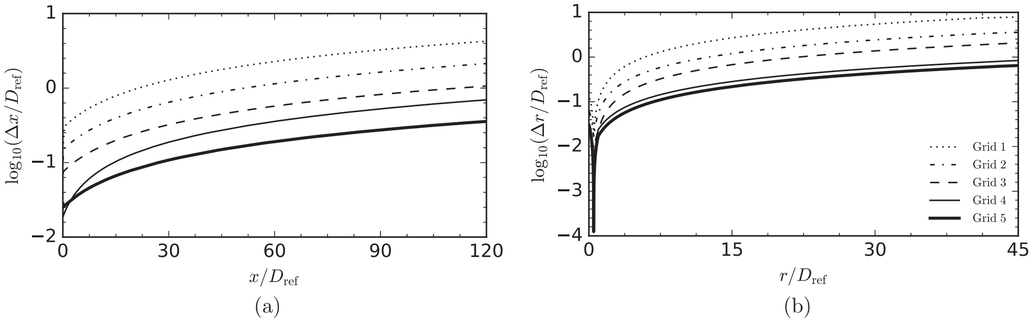

FIG. 8. Grid distribution for the turbulent jet simulations, showing grid spacing as a function of spatial distance for (a) axial and (b) radial direction. The azimuthal discretization is uniform for all cases.

quantities of normalized axial velocity, mixture fraction, and temperature are shown in Fig. 9. The simulation results for the finer grids agree favorably with experiments. Once the simulation is statistically stationary, the Lyapunov exponent is calculated following the process outline in Sec. II B and Table I. Since the Lyapunov exponent is a measure for the short-time dynamics of a system and does not rely on statistical information, an important aspect is the reduced computational cost for its evaluation. For the grid 4 inert case, two simulations, running for approximately 60 nondimensional times, are required to calculate the Lyapunov exponent. In comparison, to obtain the statistics presented in Fig. 9, statistics were collected over approximately 1500 nondimensional times, which corresponds to an increase of computational cost by 1250%.

The ratio between turbulent and molecular viscosity is shown in Fig. 10. From these results, it can be seen that the region of highest turbulence is aligned with the shear layer. For the reacting jet simulation on the coarse mesh (grid 1), the shear layer shows regions in which this viscosity ratio exceeds values of 30. For grid 2, this ratio reduces to maximum values around 11 and becomes less than 8 for the finer grids. One effect of the large turbulent viscosity in the coarsest grid is that the flame height, which is determined by the location of the stoichiometric mixture fraction on the centerline [see Fig. 10(b)], is noticeably shorter due to faster scalar mixing compared to the solutions obtained for the finer grids. The inert jets have maximum viscosity ratios around 10 for the finer grids.

B. Effect of perturbation

The axial velocity is perturbed using Eq. (7) with $\epsilon = 10^{-8}$ and $\epsilon = 10^{-4}$ for both the inert and the reacting case using grid 3. Temporal evolutions of the normalized separation for each component of velocity and mixture fraction are shown in Fig. 11(a), and results for the corresponding reacting cases with progress variable and temperature included are shown in Fig. 11(b). For each plot the time is

TABLE V. Reference parameters for the jet flow simulation. The parameters for the inert jet simulation are slightly different from that of Ref. [45] to allow for comparison with reactive flow simulations. The minimum filter width, Δ_{min}, is computed as the cube root of the volume of the smallest cylindrical cell (which is near the nozzle lip) for the finest grid (grid 5) for each case.

Parameter	Inert jet	Reacting jet
Re	14 720	
η/D_{ref}	1.9×10^{-3}	9.3×10^{-3}
Δ_{min}/η	2.23	0.46

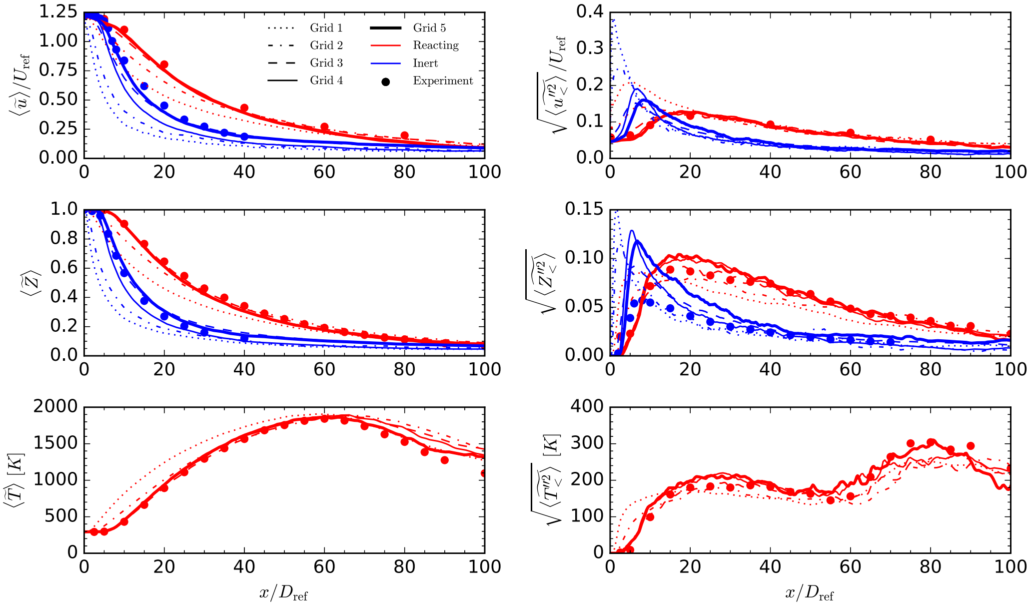

FIG. 9. Resolved center-line statistics for the inert (blue) and reacting (red) jets for axial velocity, mixture fraction, and temperature compared with experimental values [45–48]. Mean quantities on the left column, root-mean-square quantities on the right column.

nondimensionalized by the characteristic convective time scale, $\tau_{\mathrm{conv}} = D_{\mathrm{ref}}/U_{\mathrm{ref}}$. The separations, similarly to the homogeneous isotropic turbulence, grow exponentially with time until saturation.

The initial response regions differ between the velocity and the scalars. For the FPV approach, the density is interpolated from a precomputed chemistry table that is a function of the scalars. A small change in the scalars can lead to a larger change in the density which in the end affects the velocity field through continuity and momentum conservation. This effect leads to larger initial separation for the velocity field than for the scalars. This phenomenon is predominantly seen in the reacting case due to larger density differences. In the linear region, the flow-field variables become uniform, which continues until saturation. For a larger or smaller perturbation, the Lyapunov exponent remains invariant, and the linear region shrinks or extends, respectively. Tests were also performed by varying the initial time of the separation (not shown). The variation of the Lyapunov exponent is around 5% based on these analyses.

C. Effect of grid refinement

To examine the dependence of the Lyapunov exponent on the mesh resolution, simulations on five different grids are performed for the inert and reacting jets. In this study, the first four grids are generated by successively doubling the mesh resolution in all directions, grid 5 only refines the mesh resolution in axial and radial direction. Quantitative results for the Lyapunov exponent are shown in Table VI.

For the forced homogeneous isotropic turbulence configuration in Sec. IV it was observed that the Lyapunov exponent increases and reaches a maximum value once the grid is sufficiently refined. For the inert jet, the relative increase in the Lyapunov exponent is much more pronounced for the coarser grids than for the finer grids. The Lyapunov exponent more than doubles from grid 1 to 3 and doubles again from grid 3 to 4. Convergence is nearly reached after testing the even finer grid 5. Contours of the separation and of mixture fraction for each grid can be found in Fig. 12. The corresponding temporal evolutions of the separations $\|\delta Z\|$ are illustrated in Fig. 13. The separations

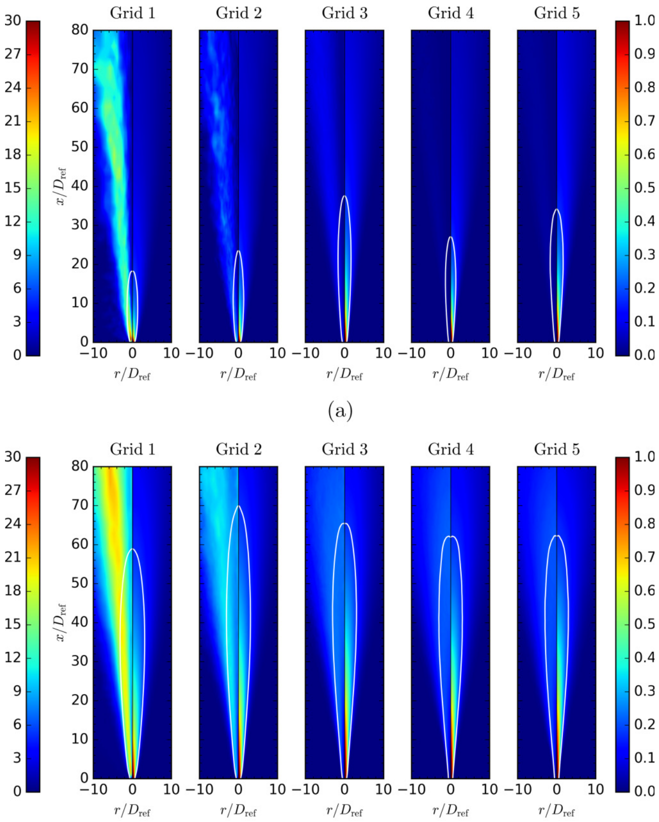

(a)

(b)

FIG. 10. Jet quality evaluation for (a) inert jet and (b) reacting jet. In each panel, on the left of the vertical line the ratio of turbulent viscosity to molecular viscosity, $\langle \nu_T \rangle / \langle \nu \rangle$, is shown; on the right the Favre-averaged mixture fraction is shown. The white line indicates the Favre-averaged stoichiometric mixture fraction with $Z_{\mathrm{st}} = 0.167$.

are present in the turbulent regions of the flow; the separation is zero in the coflow. For the reacting jet, the variation in the Lyapunov exponent is much larger between grid 1 and 2, as compared to the difference between grid 2 to 3. This means that most of the dynamics is captured in grid 2. The statistical results, presented in Fig. 9, also show this behavior: grid 2 has closer statistics to the experimental values than grid 1, and the statistical convergence is observed for grid 3 and above. These results show that grid 3 is suitable for capturing the global statistical behavior of the reacting jet, whereas at least grid 4 refinement is needed to simulate the dynamics of the inert jet. These observations are in agreement with the convergence of statistics in Fig. 9. The physical reason for these two different resolution requirements is provided in the next section. Establishing the relation between the convergence of statistics and the saturation of the Lyapunov exponent is left for future work.

D. Effect of combustion and heat release on predictability

Converting the normalized Lyapunov exponents for the finest grids into physical units, a predictability time of $t_{\mathrm{p,reac}} \approx 650\ \mu\mathrm{s}$ ($3.45\tau_{\mathrm{conv}}$) is obtained for the reacting jet, and $t_{\mathrm{p,inert}} \approx 100\ \mu\mathrm{s}$ ($0.54\tau_{\mathrm{conv}}$) is obtained for the inert jet. The physical reason for this difference is due to temperature increase by combustion and associated effects on density and viscous transport properties. A scaling of the effective Reynolds number can be calculated assuming a power law for the viscosity

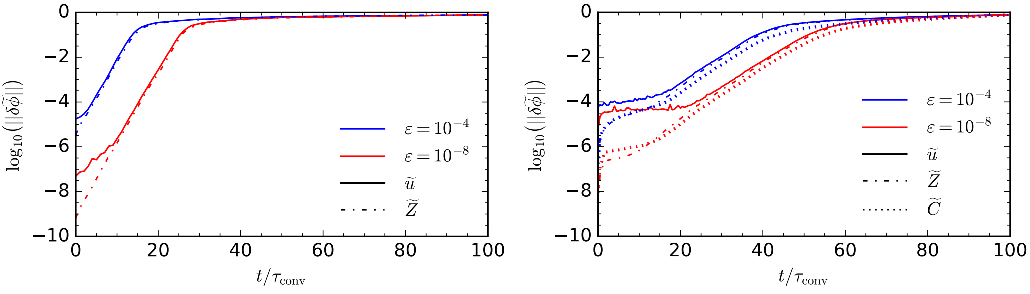

(a) (b)

FIG. 11. Normalized separations of velocity and transport variables for (a) inert jet and (b) reacting jet; axial velocity component $\widetilde{u}$ is perturbed with $\epsilon = 10^{-4}$ (blue) and $\epsilon = 10^{-8}$ (red). Simulations are performed using grid 3.

as $\mathrm{Re} = \rho U_{\rm ref} D_{\rm ref}/\mu \sim \rho(T)/\mu(T) \sim (1/T)/T^{0.7} \sim T^{-1.7}$. Considering the present configuration that is operated with a nitrogen-diluted CH_4/H_2-mixture, with an effective temperature ratio of seven: $\mathrm{Re}_{\rm react}/\mathrm{Re}_{\rm inert} = (T_a/T_{\rm ref})^{-1.7} = 0.036$. Because the jet exit Reynolds number is 14 720, the effective Reynolds number of the flame reduces by a factor of 25. Combustion laminarizes the flow field, which in turn is responsible for a slower and more predictable flow. This effect is also present in Table V. The Kolmogorov scale for the reacting jet is almost five times larger than the inert jet. As noted previously, the Lyapunov time is representative of how long it takes for nearby Eulerian fields to diverge. The actual predictability time is a function of the Lyapunov time and would be dependent on how accurate the initial conditions provided are. For an error of around 1% for the present configuration, the predictability time is expected to be around this value. With higher accuracy the predictability would become better. For example, the reacting cases simulated assume a perturbation of around 10^{-8} and have an overall predictability time of around 40 convective time scales before the separation reaches 1% of saturation (see Fig. 13).

The increased predictability of the reacting flow, due to laminarization, suggest that it may be possible to determine the predictability time of reacting flows, using a lower Reynolds number inert jet, given the proper scaling relationships. Muniz and Mungal [51] investigated inert jets at Reynolds numbers of 2000 and 10 000 and reacting flows at Reynolds numbers of 10 000 and 37 500. In their work, several important observations were made, combustion reduced the local Reynolds number by a factor of 10 over the flame and turbulence intensities by up to 40% and increased the centerline velocities by a factor of 2 to 3. In the present study, similar behavior can be observed for the reacting jet as shown in Fig. 9, suggesting the predictability of the reacting jet could be estimated based on a simple inert jet with a reduced Reynolds number. However, in practice this approach is not straightforward, as a large variation in the Reynolds number will be present due to the localized heating of the fluid. Thus, at the centerline near the nozzle the effective Reynolds number will be

TABLE VI. Comparison of Lyapunov exponent for inert and reacting jet-flow simulations. Grid numbers correspond to grids shown in Table IV.

Grid	$\lambda\tau_{\rm conv}$ (inert)	$\lambda\tau_{\rm conv}$ (reacting)
1	0.330	0.200
2	0.428	0.305
3	0.735	0.311
4	1.649	0.291
5	1.839	0.290

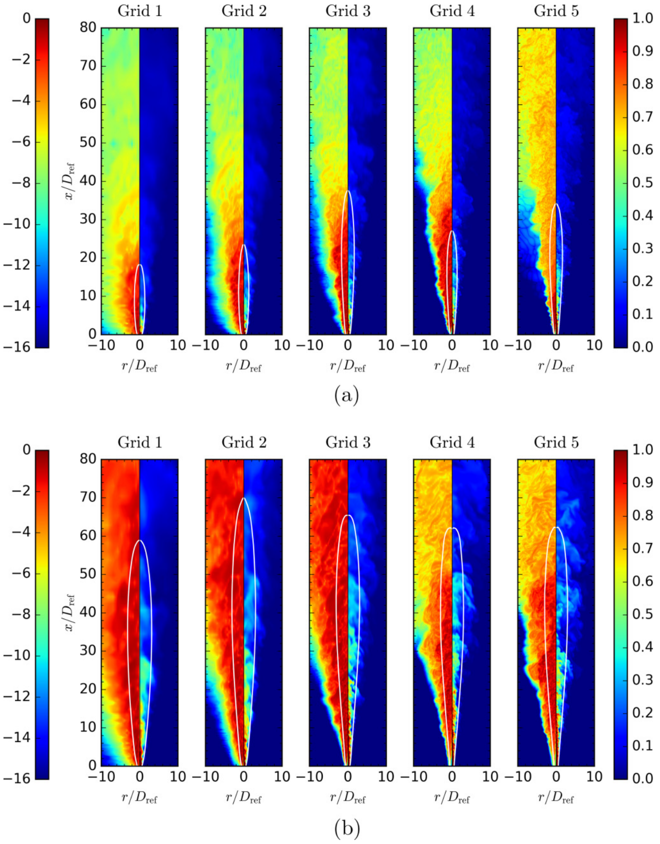

(a)

(b)

FIG. 12. Mesh refinement for (a) inert jet and (b) reacting jet. In each panel, on the left of the vertical line the logarithm of the absolute value of the instantaneous separation at saturation (at $t/\tau_{\mathrm{conv}} = 100$) is shown; on the right the instantaneous mixture fraction at the same instance is shown. The white line indicates the Favre-averaged stoichiometric mixture fraction with $Z_{\mathrm{st}} = 0.167$.

equal to that in the pipe, whereas the effective Reynolds number in the shear layer will be significantly reduced. In the work of Tacina and Dahms [52], an extension of the classical momentum diameter was developed for reacting flows, by replacing the exothermic reaction by an equivalent nonreacting flow. In this approach, the temperature of one fluid is increased based on the peak temperature and overall stoichiometry of the mixture. Good agreement of the effects of heat release were obtained in the near and far fields for momentum-dominated turbulent jet flames. A similar conclusion was obtained from the DNS study of Knaus and Pantano [53], which determined that the effects of heat release rate can be scaled by using Favre-averaged large-scale turbulence quantities for flows of moderate Reynolds numbers. However, this approach is less suited for the dissipation subrange of the temperature spectra due to the strong nonlinearities present in combustion. Following the approach proposed by Tacina and Dahms [52], the predictability of the reacting jet could be estimated based on an equivalent inert jet simulation with modified fluid temperatures. Determining the validity of this approach is beyond the scope of the current investigation and is left for future work.

E. Application of the Lyapunov exponent to determining computational domain size

The Lyapunov exponent has been shown to converge if the dynamics of the system are adequately resolved by the mesh. However, it is expected that the global dynamics of the system may also be a function of the computational domain size and shape. This is examined by computing the Lyapunov

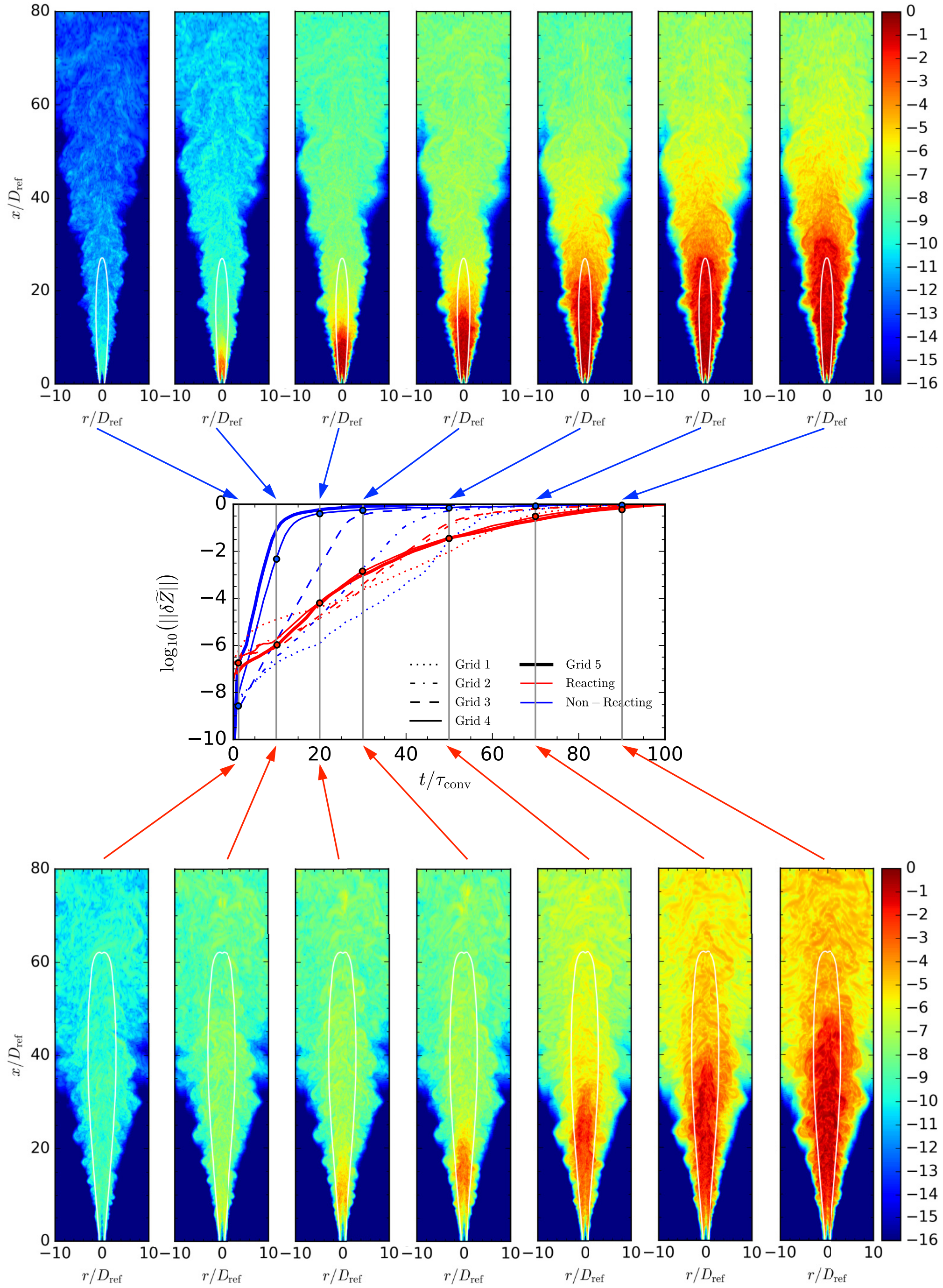

FIG. 13. Separations for each grid and case. Lyapunov exponents are presented in Table VI. The contour plots correspond to the logarithm of the absolute value of the separation for mixture fraction, $\|\delta\widetilde{Z}\|$, between two simulations for grid 4 for (top) inert jet and (bottom) reacting jet. The white line indicates the Favre-averaged stoichiometric mixture fraction with $Z_{\mathrm{st}} = 0.167$.

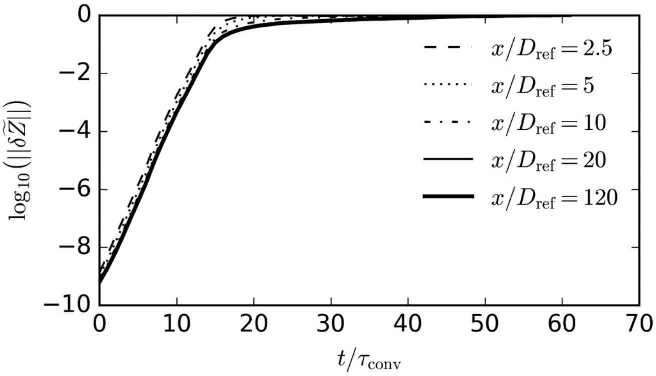

FIG. 14. Computed separation distance for different axial extends of the computational domains from $x/D_{\mathrm{ref}} = 2.5$ to $x/D_{\mathrm{ref}} = 120$.

exponent for different domain sizes for the grid 4 inert jet. Figure 14 presents the global separation for computational domains of various lengths, from $x/D_{\mathrm{ref}} = 2.5$ to 120. As can be seen in Fig. 14, the jet dynamics varies significantly over the first $20D_{\mathrm{ref}}$ of the jet. Thus, if the computational domain is reduced to a length less than $20D_{\mathrm{ref}}$, it is expected that some of the important jet dynamics will be lost. In comparison, past $r/D_{\mathrm{ref}} = 20$, smaller changes in the jet are observed. Further, since these changes are due to the diffusion and lower velocity fluctuations, it is expected that the positions downstream of this region will have a very small impact on the global separation, and thus the global Lyapunov exponent. This behavior is confirmed in Fig. 14, where the local separation converges for computational domains longer than $20D_{\mathrm{ref}}$, with a mean relative difference in the global separation of less than 11% for a domain of $20D_{\mathrm{ref}}$, when compared to the full domain. In addition, computational domains, with reduced radial length were also compared with the trends agreeing with those of reducing the axial length.

In addition to comparing the normalized saturation curves to determine the impact of the domain size on the Lyapunov exponent, an analysis of the global saturation level is also completed. With increasing domain size, saturation is observed at a lower threshold but occurs at approximately the same time. As the current approach calculates the Lyapunov exponent based on the global separation, this behavior is consistent with the previous observations reported in the paper. If the computational domain is resolved to a significant level, and assuming that the computational domain includes the areas of high turbulence and areas which are sensitive to small perturbations, the growth of the separation is determined by the local flow conditions. Thus, increasing the computational domain does not influence the separation behavior. In comparison, the level at which saturation is observed is a strong function of the computational domain. The cause of this is that as the computational domain increases the fraction of the domain that contains areas of low turbulence or areas which are not sensitive to perturbations increases. Thus, on a global scale the average separation observed decreases resulting in saturation at a lower value. It should be noted that the following behavior is expected in physical geometries where turbulence, and thus sensitivity to small perturbation, is decaying. In processes in which strong turbulence is generated locally or develops, such as pipe flows, turbulence separation, and boundary layer formation, this behavior is not expected, and the Lyapunov exponent may retain a strong dependence on the size of the computational domain.

F. Application of the Lyapunov exponent to assess flow-dependent properties

In the previous sections, the global Lyapunov exponent was computed to determine the impact of various aspects (mesh resolution, computational domain, chemical source term, and perturbation level) on the global dynamics of the system. However, the same principle can be applied to assess local flow-dependent properties. In the current section, the Lyapunov exponent analysis is applied

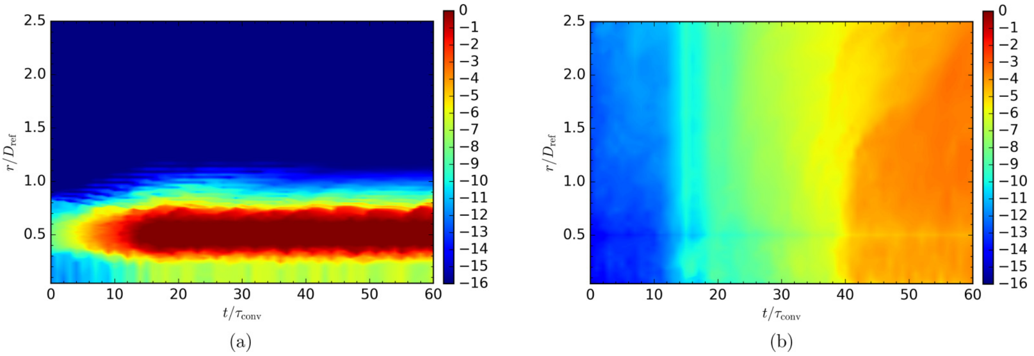

FIG. 15. Computed separation distance as a function of radial distance at two axial locations. (a) $x/D_{\mathrm{ref}} = 0.33$ and (b) $x/D_{\mathrm{ref}} = 20$.

to determine local areas of strong separation, corresponding to areas of high turbulence or high sensitivity to local conditions. Detecting such a region via the Lyapunov exponent can be used to determine local grid refinement and areas which contain interesting flow dynamics.

The time evolution of the local separation, as a function of radial location at two axial heights, one close to the nozzle at $x/D_{\mathrm{ref}} = 0.33$ and one further downstream at $x/D_{\mathrm{ref}} = 20$, is presented in Fig. 15. Several important characteristics can be observed from this figure. First, the behavior of the local separation, and conversely the Lyapunov exponent, is a strong function of radial location. In the laminar coflow, the local separation remains close to machine precision over the simulation time, indicating that the coflow is not sensitive to small changes in the initial or boundary conditions. In comparison, the dynamics in the jet core and shear layer are clearly visible in Fig. 15(a), with the core of the jet less sensitive to small perturbations as compared to the shear layer. Further, the behavior in the jet core and shear layer is relatively constant $\tau_{\mathrm{conv}} > 20$, demonstrating that saturation occurs very quickly and the separation growth is strongly dependent on the radial location near the nozzle. In comparison, further downstream at $x/D_{\mathrm{ref}} = 20$ [Fig. 15(b)], a larger portion of the jet experiences similar rates of separation. However, at this location the level at which saturation occurs is approximately four orders of magnitude lower than at $x/D_{\mathrm{ref}} = 0.33$, demonstrating that the turbulence has decayed at this location.

A second data set is calculated at two fixed radial locations, one at the centerline ($r/D_{\mathrm{ref}} = 0$) and the other one along the nozzle lip line, $r/D_{\mathrm{ref}} = 0.5$, for axial heights between $x/D_{\mathrm{ref}} = 0$ and $x/D_{\mathrm{ref}} = 60$. These results are shown in Fig. 16. Compared to the radial separation profiles,

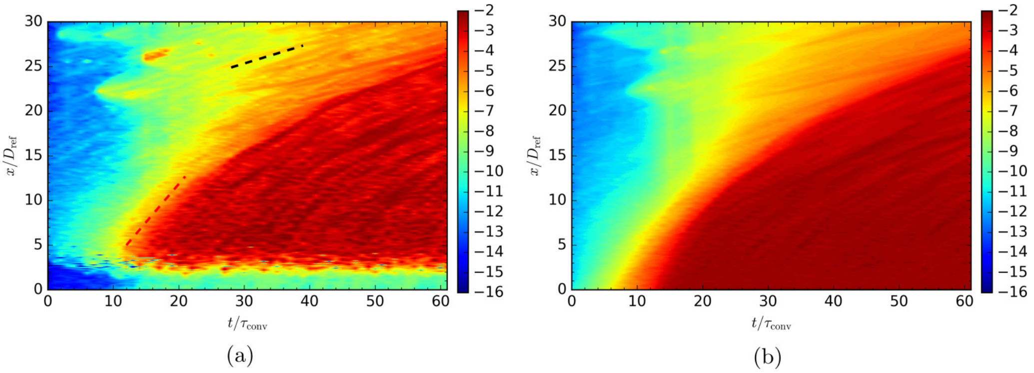

FIG. 16. Computed separation distance as a function of axial heights at two radial locations. (a) $r/D_{\mathrm{ref}} = 0$ and (b) $r/D_{\mathrm{ref}} = 0.5$.

which reach saturation very quickly, an analysis of the separation growth shows that the time required to reach saturation is a strong function of axial height. As seen in Fig. 16 the time to reach saturation increases with increased axial height. The rate of saturation growth as a function of axial height and nondimensional time, represented by the red and black dashed lines, is compared to the mean axial velocity. At both axial heights, the influence of the perturbation propagates downstream at approximately the local mean axial velocity. Thus, the Lyapunov exponent can be applied to estimate the time required for upstream turbulence to propagate downstream. This information is trivial for a simple stationary inert jet, but this process could be applied for transient simulations to distinguish between regions of turbulence generation and turbulence transport.

VI. CONCLUSIONS

A metric based on the Lyapunov exponent is proposed to characterize the dynamic content of LES and to assess the predictability time of simulations. This method is applied in simulations of forced homogeneous isotropic turbulence and reacting and inert turbulent jets. It is shown that the chaotic dynamics of DNS and LES calculations of isotropic, anisotropic, reacting, and inert flows behaves like simple low-dimensional chaotic systems, such as the Lorenz system. The inverse of the Lyapunov exponent provides an estimate of the predictability time of a system, which is useful information in predicting rapid dynamic phenomena. The Lyapunov exponent asymptotically approaches a limit as the filter width decreases in size.

For small perturbations, the predictability of the reacting and inert flow cases scales with the Kolmogorov time scales and becomes comparable to the integral time scale of the system under investigation. For the jet-flow simulations, it was shown that combustion makes the jet dynamics more predictable in two ways. First, it enlarges the initial response time, which is the time that the exponential divergence of the chaotic dynamics takes to begin. Second, the exponential growth rate of the chaotic dynamics is lower due to the flame relaminarization, which decreases the effective Reynolds number.

An analysis of the local Lyapunov exponent demonstrates that this metric can also determine flow-dependent properties, such as areas of high turbulence and areas which are sensitive to small perturbations within the flow field. This information can be used to indicate areas where local grid refinement may be required. In addition, the impact of flow-dependent properties on the evolution of the flow can be assessed using the Lyapunov exponent and corresponding separation between two simulations. This information can provide an indication of the sensitivity of the simulation to initial conditions and boundary conditions, which may be important for the simulation of transient events. Finally, it is demonstrated that the global Lyapunov exponent can be utilized as a metric to determine if the computational domain is large enough to capture the dynamic nature of the flow. For the inert jet, the Lyapunov analysis correctly predicts that the area which contains the majority of the dynamics is located close to the nozzle. It is observed that outside of this area the flow does not have a significant impact on the dynamic nature of the system as measured by the Lyapunov exponent.

The Lyapunov metric is self-contained and model-free, which means it is consistent with the LES model adopted and does not require estimates for the subgrid kinetic energy. Since this metric probes the short-time dynamics of unsteady flow-field simulations, it complements currently employed statistical metrics that are difficult to apply in nonstationary flows. As such, the method is directly applicable to any LES calculation, easy to implement, and only requires a short-time simulation to extract meaningful results. Furthermore, the Lyapunov metric can be used as a sensitivity parameter to assess the impact of combustion models, chemical mechanisms, subgrid closures, and numerical discretization on the short-term dynamic behavior of a particular flow-field simulation. One shortcoming of the Lyapunov exponent, however, is that its asymptotic value is not known *a priori*, and simulations on successively refined meshes or different submodels are necessary to assess the quality of particular numerical simulations.

This analysis provides a metric to determine the effect of the smallest scales on the flow dynamics, which is particularly relevant for examining deterministic rare or intermittent events in turbulent flow simulations, such as local extinction and reignition events in turbulent flames [54], engine knock and preignition in internal combustion engines [55], or transition, separation, and intermittency in turbulent flows [56]. If the events have a stochastic nature, the proposed Lyapunov-exponent analysis has to be extended to relax the assumption on determinism. This is left for future work.

ACKNOWLEDGMENTS

Financial support through the Ford-Stanford Alliance Project No. C2015-0590 is gratefully acknowledged. Computational resources supporting this work were provided by the National Energy Research Scientific Computing Center, a DOE Office of Science User Facility supported by the Office of Science of the US Department of Energy under Contract No. DE-AC02-05CH11231.

[1] S. B. Pope, Ten questions concerning the large-eddy simulation of turbulent flows, New J. Phys. **6**, 35 (2004).

[2] I. B. Celik, Z. N. Cehreli, and I. Yavuz, Index of resolution quality for large eddy simulations, J. Fluid Eng. **127**, 949 (2005).

[3] L. Vervisch, P. Domingo, G. Lodato, and D. Veynante, Scalar energy fluctuations in large-eddy simulation of turbulent flames: Statistical budgets and mesh quality criterion, Combust. Flame **157**, 778 (2010).

[4] B. J. Geurts and J. Fröhlich, A framework for predicting accuracy limitations in large-eddy simulation, Phys. Fluids **14**, L41 (2002).

[5] A. Robert, L. Martinez, J. Tillou, and S. Richard, Eulerian-Eulerian large eddy simulations applied to non-reactive transient diesel sprays, Oil Gas Sci. Technol. **69**, 141 (2013).

[6] Y. C. See and M. Ihme, Large eddy simulation of a partially-premixed gas turbine model combustor, Proc. Combust. Inst. **35**, 1225 (2015).

[7] G. Boudier, G. Staffelbach, L. M. Y. Gicquel, and T. Poinsot, Mesh dependency of turbulent reacting large-eddy simulations of a gas turbine combustion chamber, in *Quality and Reliability of Large-Eddy Simulations*, edited by J. Meyers, B. J. Geurts, and P. Sagaut (Springer, New York, 2008), pp. 319–330.

[8] C. Chnafa, S. Mendez, and F. Nicoud, Image-based large-eddy simulation in a realistic left heart, Comput. Fluids **94**, 173 (2014).

[9] P. Gousseau, B. Blocken, and G. J. F. van Heijst, Quality assessment of large-eddy simulation of wind flow around a high-rise building: Validation and solution verification, Comput. Fluids **79**, 120 (2013).

[10] K. A. Kemenov, H. Wang, and S. B. Pope, Turbulence resolution scale dependence in large-eddy simulations of a jet flame, Flow, Turb. Combust. **88**, 529 (2011).

[11] D. You and P. Moin, A dynamic global-coefficient subgrid-scale eddy-viscosity model for large-eddy simulation in complex geometries, Phys. Fluids **19**, 065110 (2007).

[12] D. Ruelle, Ergodic theory of differentiable dynamical systems, Public. Math. Inst. Hautes Études Scientif. **50**, 27 (1979).

[13] J. D. Farmer, E. Ott, and J. A. Yorke, The dimension of chaotic attractors, Phys. D **7**, 153 (1983).

[14] J. P. Eckmann and D. Ruelle, Ergodic theory of chaos and strange attractors, Rev. Mod. Phys. **57**, 617 (1985).

[15] R. C. Hilborn, *Chaos and Nonlinear Dynamics* (Oxford University Press, Oxford, 1994).

[16] G. Boffetta, M. Cencini, M. Falcioni, and A. Vulpiani, Predictability: A way to characterize complexity, Phys. Rep. **356**, 367 (2002).

[17] I. Goldhirsch, P.-L. Sulem, and S. A. Orszag, Stability and Lyapunov stability of dynamical systems: A differential approach and a numerical method, Phys. D **27**, 311 (1987).

[18] C. E. Leith and R. H. Kraichnan, Predictability of turbulent flows, J. Atmos. Sci. **29**, 1041 (1972).

[19] S. Kida, M. Yamada, and K. Ohkitani, Error growth in a decaying two-dimensional turbulence, J. Phys. Soc. Jpn. **59**, 90 (1990).

[20] E. Aurell, G. Boffetta, A. Crisanti, G. Paladin, and A. Vulpiani, Growth of Noninfinitesimal Perturbations in Turbulence, Phys. Rev. Lett. **77**, 1262 (1996).

[21] J. Harlim, M. Oczkowski, J. A. Yorke, E. Kalnay, and B. R. Hunt, Convex Error Growth Patterns in a Global Weather Model, Phys. Rev. Lett. **94**, 228501 (2005).

[22] U. Frisch, Fully developed turbulence and intermittency, Ann. NY Acad. Sci. **357**, 359 (1980).

[23] L. Keefe, P. Moin, and J. Kim, The dimension of attractors underlying periodic turbulent Poiseuille flow, J. Fluid Mech. **242**, 1 (1992).

[24] A. Crisanti, M. H. Jensen, A. Vulpiani, and G. Paladin, Intermittency and Predictability in Turbulence, Phys. Rev. Lett. **70**, 166 (1993).

[25] E. Aurell, G. Boffetta, A. Crisanti, G. Paladin, and A. Vulpiani, Predictability in systems with many characteristic times: The case of turbulence, Phys. Rev. E **53**, 2337 (1996).

[26] E. Aurell, G. Boffetta, A. Crisanti, G. Paladin, and A. Vulpiani, Predictability in the large: An extension of the concept of Lyapunov exponent, J. Phys. A **30**, 1 (1997).

[27] E. N. Lorenz, Atmospheric predictability as revealed by naturally occurring analogues, J. Atmos. Sci. **26**, 636 (1969).

[28] G. Paladin and A. Vulpiani, Predictability in spatially extended systems, J. Phys. A: Math. Gen. **27**, 4911 (1994).

[29] R. Temam, *Infinite-Dimensional Dynamical Systems in Mechanics and Physics*, 2nd ed. (Springer, New York, 1997).

[30] V. I. Oseledets, A multiplicative ergodic theorem. Characteristic Ljapunov, exponents of dynamical systems, Tr. Mosk. Mat. Obs. **19**, 179 (1968).

[31] M. Germano, U. Piomelli, P. Moin, and W. H. Cabot, A dynamic subgrid-scale eddy viscosity model, Phys. Fluids A **3**, 1760 (1991).

[32] C. D. Pierce and P. Moin, Progress-variable approach for large-eddy simulation of non-premixed turbulent combustion, J. Fluid Mech. **504**, 73 (2004).

[33] M. Ihme, C. M. Cha, and H. Pitsch, Prediction of local extinction and re-ignition effects in non-premixed turbulent combustion using a flamelet/progress variable approach, Proc. Combust. Inst. **30**, 793 (2005).

[34] C. D. Pierce and P. Moin, A dynamic model for subgrid-scale variance and dissipation rate of a conserved scalar, Phys. Fluids **10**, 3041 (1998).

[35] M. Ihme and H. Pitsch, Prediction of extinction and reignition in non-premixed turbulent flames using a flamelet/progress variable model. 2. A posteriori study with application to Sandia flames D and E, Combust. Flame **155**, 90 (2008).

[36] M. Ihme, H. Pitsch, and D. Bodony, Radiation of noise in turbulent non-premixed flames, Proc. Combust. Inst. **32**, 1545 (2009).

[37] B. A. Rankin, M. Ihme, and J. P. Gore, Quantitative model-based imaging of mid-infrared radiation from a turbulent nonpremixed jet flame and plume, Combust. Flame **162**, 1275 (2015).

[38] C. Rosales and C. Meneveau, Linear forcing in numerical simulations of isotropic turbulence: Physical space implementations and convergence properties, Phys. Fluids **17**, 095106 (2005).

[39] M. R. Petersen and D. Livescu, Forcing for statistically stationary compressible isotropic turbulence, Phys. Fluids **22**, 116101 (2010).

[40] P. L. Johnson and C. Meneveau, Large-deviation joint statistics of the finite-time Lyapunov spectrum in isotropic turbulence, Phys. Fluids **27**, 085110 (2015).

[41] T. S. Lundgren, Linearly forced isotropic turbulence, Center for Turbulence Research, Annu. Res. Briefs, 461–473 (2003).

[42] P. Mohan, N. Fitzsimmons, and R. Moser, Scaling of Lyapunov exponents in homogeneous, isotropic turbulence, APS Division of Fluid Dynamics, abstract R19.010 (2015).

[43] M. T. Rosenstein, J. J. Collins, and C. J. De Luca, A practical method for calculating largest Lyapunov exponents from small data sets, Phys. D **65**, 117 (1993).

[44] V. Eswaran and S. B. Pope, An examination of forcing in direct numerical simulations of turbulence, Comput. Fluids **16**, 257 (1988).

[45] J. Mi, D. S. Nobes, and G. J. Nathan, Influence of jet exit conditions on the passive scalar field of an axisymmetric free jet, J. Fluid Mech. **432**, 91 (2001).

[46] V. Bergmann, W. Meier, D. Wolff, and W. Stricker, Application of spontaneous Raman and Rayleigh scattering and 2D LIF for the characterization of a turbulent CH4/H2/N2 jet diffusion flame, Appl. Phys. B **66**, 489 (1998).

[47] W. Meier, R. S. Barlow, Y. L. Chen, and J.-Y. Chen, Raman/Rayleigh/LIF measurements in a turbulent $CH_4/H_2/N_2$ jet diffusion flame: Experimental techniques and turbulence-chemistry interaction, Combust. Flame **123**, 326 (2000).

[48] C. Schneider, A. Dreizler, J. Janicka, and E. P. Hassel, Flow field measurements of stable and locally extinguishing hydrocarbon-fueled jet flames, Combust. Flame **135**, 185 (2003).

[49] C. T. Bowman, R. K. Hanson, D. F. Davidson, W. C. Gardiner, V. Lissianski, G. P. Smith, D. M. Golden, M. Frenklach, and M. Goldenberg, GRI-Mech 2.11, 1997, http://www.me.berkeley.edu/gri-mech/

[50] P. S. Kothnur, M. S. Tsurikov, N. T. Clemens, J. M. Donbar, and C. D. Carter, Planar imaging of CH, OH, and velocity in turbulent non-premixed jet flames, Proc. Combust. Inst. **29**, 1921 (2002).

[51] L. Muñiz and M. G. Mungal, Effects of heat release and buoyancy on flow structure and entrainment in turbulent nonpremixed flames, Combust. Flame **126**, 1402 (2001).

[52] K. M. Tacina and W. J. A. Dahm, Effects of heat release on turbulent shear flows. Part 1. A general equivalence principle for non-buoyant flows and its application to turbulent jet flames, J. Fluid Mech. **415**, 23 (2000).

[53] R. Knaus and C. Pantano, On the effect of heat release in turbulence spectra of non-premixed reacting shear layers, J. Fluid Mech. **626**, 67 (2009).

[54] R. S. Barlow and J. H. Frank, Effects of turbulence on species mass fractions in methane/air jet flames, Proc. Combust. Inst. **27**, 1087 (1998).

[55] C. Dahnz and U. Spicher, Irregular combustion in supercharged spark ignition engines: Pre-ignition and other phenomena, Int. J. Engine Res. **11**, 485 (2010).

[56] H. Tennekes and J. L. Lumley, *A First Course in Turbulence* (MIT Press, Cambridge, MA, 1972).